Dissipationless dynamics of spin supersolid states in a spin-1/2 triangular antiferromagnet with impurities

Yixuan Huang,[1] Yuan Gao,[2, 3] Wei Li,[3, 4] Seiji Yunoki,[1, 5, 6, 7] and Sadamichi Maekawa[1, 8]

[1]*RIKEN Center for Emergent Matter Science (CEMS), Wako 351-0198, Japan*
[2]*School of Physics, Beihang University, Beijing 100191, China*
[3]*Institute of Theoretical Physics, Chinese Academy of Sciences, Beijing 100190, China*
[4]*Peng Huanwu Collaborative Center for Research and Education, Beihang University, Beijing 100191, China*
[5]*RIKEN Center for Computational Science (R-CCS), Kobe 650-0047, Japan*
[6]*RIKEN Center for Quantum Computing (RQC), Wako 351-0198, Japan*
[7]*RIKEN Pioneering Research Institute (PRI), Wako 351-0198, Japan*
[8]*Advanced Science Research Center, Japan Atomic Energy Agency, Tokai 319-1195, Japan*
(Dated: October 2, 2025)

Motivated by recent experimental observations of the possible spin supersolid states in triangular lattice compounds, we study the dynamical properties of various ground states in the spin-1/2 easy-axis antiferromagnetic Heisenberg model with impurities under magnetic fields using numerical methods. In both low- and high-field spin supersolid states, the gapless Goldstone mode at the K points remains robust against impurities, which is related to the presence of spin superfluidity. By contrast, we find that impurities induce a splitting of the magnon bands at the same density level in the conventional magnetic state, the so-called up-up-down state. In addition, the finite superfluid stiffness probed by the twisted phase in the spin supersolid states is consistent with the excitation spectrum. We argue that this excitation spectrum with impurity provides direct evidence for the dissipationless dynamics in the spin supersolid states, which could be tested in neutron scattering experiments.

Introduction. — The supersolid features coexisting superfluidity and spatial symmetry breaking order which is originally proposed as an exotic quantum state in solid Helium [1–5]. Recently, distinctive manifestation of the supersolidity has also been discovered in the ultracold quantum gases, resulting in the dipolar supersolid [6–16]. Given the fact that the boson models can be mapped onto the spin models, the spin supersolid may exist in frustrated spin systems, with the triangular lattice Heisenberg antiferromagnets as the most promising platform [17–28]. To this end, previous numerical studies [29–32] have shown spin supersolid states in the weak and strong magnetic field regimes, and an up-up-down (UUD) state between them. The phase diagram by tuning magnetic fields has been mapped out both at zero

and finite temperatures [29, 32].

The triangular compound $Na_2BaCo(PO_4)_2$, which was extensively studied as a candidate for quantum spin liquids [33–38], has attracted further interest recently because of the potential realization of spin supersolid states under magnetic fields [32, 39–47]. In particular, a giant magnetocaloric effect is observed in the critical regime [40] which promotes high-performance demagnetization cooling [44, 48], and the phase diagram agrees well with the numerical studies of the spin-1/2 anisotropic triangular Heisenberg model. Thus, this material provides an ideal platform to explore the spin supersolid states. Further exciting progress from inelastic neutron scattering experiments shows the low-energy excitations with rotonlike minimum at the M points and gapless Goldstone modes at the K points [41, 47], both of which are consistent with the dynamical spin structure factor calculated with unbiased numerical approaches [31, 41, 47]. However, such rotonlike minimum can also exist in quantum spin liquids [49, 50] that the spin supersolid state might be close to [51]. Despite extensive efforts, direct experimental observation of the superfluidity in the spin supersolid states remains an open question.

One of the key characteristics of superfluidity is the dissipationless dynamics that results from the scattering of the spin supercurrent [52, 53]. Indeed, recent spin current studies through the spin Seebeck effect have revealed a saturating supercurrent at low temperatures [54, 55] and a long-distance transport of the thermally induced spin current [54]. However, the incoherent magnons might also be injected into the system through the thermal methods that lead to condensation. On the other hand,
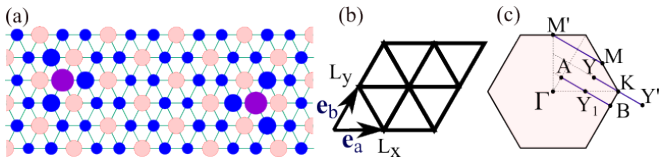

FIG. 1. Panel (a) shows the triangular lattice with blue solid circles representing positive spin values, and red shaded circles representing negative spin values. The purple solid circles represent the impurity sites with a positive spin value. The radius represents the magnitude where the purple ones have $\langle S_i^z \rangle \approx 0.5$. The ground state is obtained at $h_z = 0.836$ on the $N = 48 \times 6$ lattice where only the middle part is shown. Panel (b) shows the illustration of a triangular lattice. Panel (c) shows the corresponding Brillouin zone and momentum cuts for the dynamical spin structure factor.

the scattering due to spin supercurrent is independent of local impurities, and the low-energy excitations in the dynamical spin structure factor would remain the same in the presence of impurities. In particular, the robust Goldstone mode at the K points against impurities is directly related to the superfluid density. By contrast, for the UUD state the impurities could drastically change the low-energy spectrum.

Motivated by the recent experimental realization of spin supersolids, we numerically study the spin-1/2 anisotropic triangular Heisenberg model with magnetic fields. We show consistent results of the superfluid stiffness in the supersolid phases at both zero temperature and finite temperature, which could guide experimental searches for the signals of dissipationless dynamics due to spin superfluidity. Most importantly, we propose that the dissipationless dynamics could be identified by the dynamical spin structure factor which shows the robust gapless Goldstone mode even with impurities, which is in sharp contrast to the UUD phase where impurities induce a splitting of the magnon bands at the K points at the same density level. The dynamical spin structure factor may be measured in inelastic neutron scattering experiments where the impurities are introduced through the element substitution.

Model and methods.— We study the spin-1/2 easy-axis antiferromagnetic Heisenberg model on a triangular lattice, where the Hamiltonian is defined as

$$H = J \sum_{\langle ij \rangle} (S_i^x S_j^x + S_i^y S_j^y + \Delta_z S_i^z S_j^z) - h_z \sum_i S_i^z. \quad (1)$$

Here $\langle ij \rangle$ refers to the nearest neighbor sites and J is set to 1 as the energy unit. To be applicable to the compound $Na_2BaCo(PO_4)_2$, we set $\Delta_z/J = 1.68$ which is determined in Ref. [32] by fitting the experimental data of magnetic specific heat and magnetic susceptibility.

The magnetic impurities are approximated by the weakened bond interactions between the impurity sites and their nearest neighbor sites. The impurity Hamiltonian is defined as

$$H_{\text{imp}} = -\lambda J \sum_{\langle i_0 j \rangle} (S_{i_0}^x S_j^x + S_{i_0}^y S_j^y + \Delta_z S_{i_0}^z S_j^z), \quad (2)$$

where $\{i_0\}$ refers to the impurity sites that are evenly distributed in the lattice as illustrated in Fig. 1(a); see Supplemental Material (SM) [56] for more details. The total Hamiltonian becomes $H_{\text{total}} = H + H_{\text{imp}}$. When $\lambda = 1$, the impurity sites do not interact with the rest of the lattice which corresponds to a vacancy. In practice, we choose $\lambda = 0.95$ for numerical stability, and we find that the results are almost the same for $\lambda > 0.9$.

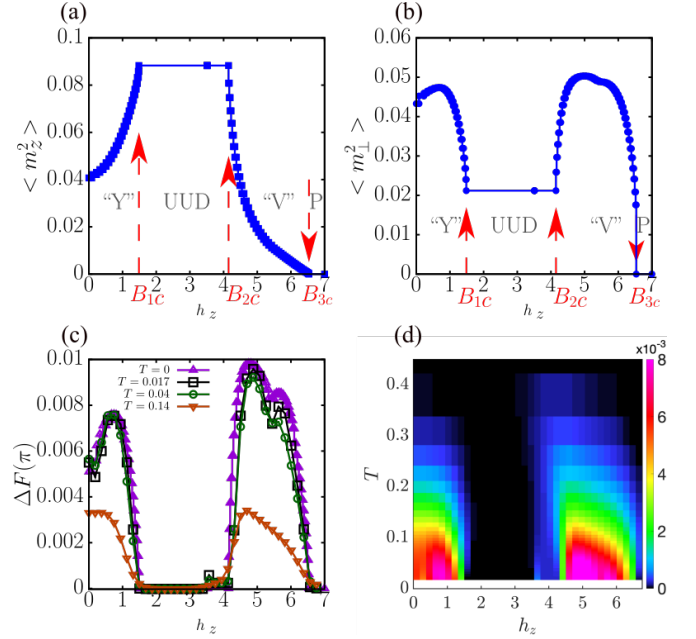Ground states at zero temperature are obtained by finite U(1) Density Matrix Renormalization Group

FIG. 2. Panels (a) and (b) show the $\langle m_z^2 \rangle$ and $\langle m_\perp^2 \rangle$ for various h_z, respectively. P refers to the polarized state. Panel (c) shows the superfluid stiffness as a function of h_z, obtained at zero and finite temperatures T. Panel (d) shows the finite T results of $\Delta F(\pi)$. The $\Delta F(\pi)$, T and h_z are normalized by J. All results are obtained on $L_y = 6$ lattices.

(DMRG) methods [57–59]. As illustrated in Fig. 1(b), the finite lattice has an open boundary in the e_a or x direction and a periodic boundary condition in the e_b or y direction with L_x and L_y sites, respectively. The total number of sites is $N = L_x \times L_y$. We mainly focus on the results on lattices with $L_y = 6$ and keep up to bond dimensions of 1400 to obtain ground states with numerical truncation error $\epsilon \lesssim 10^{-6}$. For $L_y = 9$ we use $D = 2000$ bond dimensions for the ground states with $\epsilon \lesssim 10^{-5}$.

The time evolution is implemented using the time-dependent variational principle (TDVP) for both real and imaginary time [60–62]. For real time dynamics of ground states, we employ the one-site TDVP scheme with an enlarged bond dimension achieved via global Krylov vectors [63]. $D = 2200$ are used to simulate the time up to $\tau_{tot} = 50/J$.

For finite temperature calculations, we employ imaginary time evolution using thermal tensor network [62, 64] to construct the density matrix $\rho(\beta) \equiv e^{-\beta H}$ [65]. Simulations were performed on $N = 18 \times 6$ cylinders. We retain $D = 2000$ bond states, implement U(1) symmetry, and achieve a truncation error of $\epsilon \lesssim 5 \times 10^{-5}$. The bond dimension is enlarged through the controlled bond expansion algorithm [66, 67].

Superfluid stiffness.— The phase diagram for finite magnetic fields at zero temperature has been carried out in previous studies [29, 32, 39, 40] for the easy-axis triangular antiferromagnetic Heisenberg model showing a "Y"

supersolid state, an UUD state, a "V" supersolid state, and a polarized state. These states are characterized by $\langle m_z^2 \rangle$ and $\langle m_\perp^2 \rangle$ [22], which are related to the Bragg peaks of the spin structure factor at K points via $\langle m_z^2 \rangle = S^z(\mathbf{K})/L_y^2 = \frac{1}{L_y^4}\sum_{i,j} e^{i\mathbf{K}\cdot(\mathbf{r}_i-\mathbf{r}_j)}\langle S_i^z S_j^z\rangle$ and $\langle m_\perp^2 \rangle = S^{xy}(\mathbf{K})/L_y^2 = \frac{1}{L_y^4}\sum_{i,j} e^{i\mathbf{K}\cdot(\mathbf{r}_i-\mathbf{r}_j)}\langle S_i^x S_j^x + S_i^y S_j^y\rangle$, where the summation is over the middle $L_y \times L_y$ sites. As shown in Figs. 2(a) and (b), $\langle m_z^2 \rangle$ and $\langle m_\perp^2 \rangle$ are finite in the supersolid states, and simultaneously reach maximum and minimum in the UUD states between $B_{1c} \approx 1.49$ and $B_{2c} \approx 4.15$, respectively. Above $B_{3c} \approx 6.54$ the state becomes polarized. This is consistent with previous work. The finite $\langle m_\perp^2 \rangle$ in the UUD state results from the quantum fluctuations and it becomes smaller on the wider $L_y = 9$ lattice; see SM [56] for more details.

The superfluid density in the spin supersolid states can be established by the superfluid stiffness ρ_s, which is probed by a twisted phase θ inserted through the cylinder that adds a phase factor $S_i^+ S_j^- \to e^{i\theta} S_i^+ S_j^-$ to the spin flip terms across the y boundary. The ρ_s can be approximated by

$$\rho_s = \lim_{\theta\to 0}\frac{\partial^2 F(\theta)}{\partial\theta^2} \propto F(\pi) - F(0) \equiv \Delta F(\pi) \qquad (3)$$

where $F(\theta)$ is the free energy for a given θ defined as $F = -\frac{1}{\beta}\log Z$ where $Z = \text{Tr}[\rho(\beta/2)\rho^\dagger(\beta/2)]$, and at zero temperature it is equivalent to the ground state energy $E_0(\theta)$. We choose $\theta = \pi$ where the energy difference is orders of magnitude larger than numerical accuracy; see more discussion in SM [56]. As shown in Fig. 2(c), for zero temperature the $\Delta F(\pi) = \Delta E_0(\pi)$ increases with the magnetic field in the "Y" supersolid phase, and decreases to zero as the phase approaches the UUD. A peak value of $\Delta E_0(\pi)$ is obtained around $h_z/J = 0.836$ in the "Y" state. At higher fields, the $\Delta E_0(\pi)$ becomes finite in the "V" supersolid state with a peak around $h_z/J = 4.82$ before vanishing for $h_z/J > 6.54$ in the polarized state. A small kink is identified around $h_z/J = 5.5$ in both $\Delta E_0(\pi)$ and $\langle m_\perp^2 \rangle$ which is also observed on wider $L_y = 9$ lattices; see more details in SM [56].

To examine whether the superfluid density remains finite in experimentally accessible temperatures, we obtain the $\Delta F(\pi)$ at finite temperatures. As shown in Fig. 2(c), at low temperatures the evolution of $\Delta F(\pi)$ is qualitatively the same as the one at zero temperature, and the $\Delta F(\pi)$ becomes much smaller for higher temperatures. For both "Y" and "V" states, the maximum value of $\Delta F(\pi)$ appears at the same h_z for both zero and finite temperatures. In the finite temperature results of Fig. 2(d), the domes of finite $\Delta F(\pi)$ indicate the "Y" and "V" states, which is consistent with the classical picture [32]. The two domes are separated by the UUD phase where $\Delta F(\pi)$ remains zero within the numerical
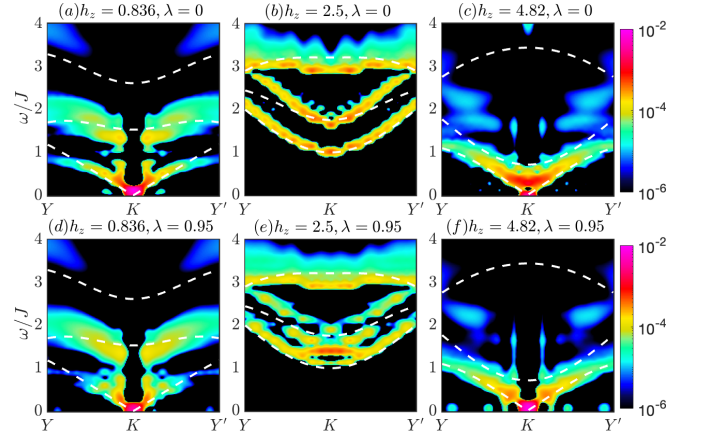

FIG. 3. The dynamical structure factor near K points. Panels (a) and (d) are obtained in the "Y" supersolid phase. Panels (b) and (e) are obtained in the UUD phase. Panels (c) and (f) are obtained in the "V" supersolid phase. Panels (a), (b), and (c) are obtained without the impurities, while panels (d), (e), and (f) are obtained with the impurities. The white dashed lines represent the dispersions from linear spin wave theory; see more details in the Supplemental Material [56].

accuracy. The $\Delta F(\pi)$ persists up to $T/J \approx 0.1$ in the spin supersolid states; see more details in SM [56].

Dynamical spin structure factor in the presence of impurities.— The dynamical spin structure factor is directly accessible in neutron scattering experiments. Because of the finite anisotropy in the Hamiltonian, it is convenient to study the transverse dynamical spin structure factor [31, 49] where the gapless Goldstone mode at K points is directly related to the superfluid density. The transverse dynamical structure factor is defined as

$$\chi(\mathbf{q},\omega) = \frac{1}{N_{mid}^2}\sum_{i,j}\int_0^{\tau_{tot}} d\tau e^{i\omega\tau - \eta\tau} e^{-i\mathbf{q}\cdot(\mathbf{r}_j-\mathbf{r}_i)}\times \qquad (4)$$
$$< \psi_0|S_i^+(\tau)S_j^- + S_i^-(\tau)S_j^+|\psi_0 > .$$

To avoid the finite boundary effect, the summation is chosen to be over the bulk $N_{mid} = \frac{3}{4}L_x \times L_y$ sites. A smearing factor of $e^{-\eta\tau}$ is applied due to finite time evolution, and the Fourier transform to ω space is followed by the Fourier transform to momentum space. We compare the dynamical spin structure factor of the original Hamiltonian with the one including finite number of impurities. As the impurity density increases to 1.85%, a clear difference can be observed in the spectrum for the UUD state while the low energy excitations for both supersolid states remain the same. This impurity density level is experimentally accessible via element substitution such as the high-temperature solution growth [68, 69] or high pressure growth methods [70–72]. We also notice that the superfluid stiffness has a slight decrease as the impurity density increases but it remains finite, which is expected because the spin supersolid state retains [73];

3

see more details in SM [56].

To provide further theoretical understanding of the dynamical spin structure factor, we obtain linear spin wave theory results that can capture the low energy excitations and the isolated magnon branches. Without impurity, the semiclassical ground state contains a three-site unit cell, where the classical spin configuration is obtained by minimizing the energy before performing the Holstein-Primakoff transformation [74]; see more details in SM [56].

Figures 3(a) and (c) show the $\chi(\mathbf{q}, \omega)$ near the K points obtained in the "Y" supersolid and "V" supersolid state, respectively. The paths in the Brillouin zone are illustrated in Fig. 1(c). The supersolid states exhibit gapless Goldstone modes from spontaneous U(1) symmetry breaking at the K points with high concentration of the spectral weight while the UUD state only has gapped spin excitations, which is consistent with previous results [31, 49, 75, 76]. This is the key feature related to the superfluidity, and is consistent with the lowest magnon branch from the linear spin wave theory. In the presence of finite impurities, the gapless mode at the K points remains robust, as shown in Figs. 3(d) and (f) for the "Y" and "V" states, respectively. This is in contrast to usual gapless states where the lowest energy excitations are affected the most by disorder or impurity, and it indicates the dissipationless dynamics as an intrinsic property associated with the spin supersolid states. Interestingly, we observe a small gapped mode in the "V" state near the K points, as shown in Fig. 3(c). This may relate to the pseudo-Goldstone mode that results from the three-fold degeneracy of the diagonal order via the order-by-quantum-disorder mechanism [77]. The three-fold degeneracy refers to $\uparrow\uparrow\downarrow$, $\uparrow\downarrow\uparrow$, and $\downarrow\uparrow\uparrow$ in a three-site unit cell. This pseudo-Goldstone mode has also been observed in the zero-field "Y" state [41] with a smaller gap, where the ground state has six-fold degeneracy. However, it is not shown in the "Y" state in Fig. 3(a) which may result from the finite numerical resolution of the spectrum. With impurities we find that the gapped mode near the K points in the "V" state disappears in Fig. 3(f), as the impurities break the degeneracy of the diagonal order.

As a comparison, we obtain the spectrum in the UUD state. As shown in Fig. 3(b), there is no continuum excitation spectrum in the UUD state. Because all spins align in the z direction in the ground state, the magnons are excited in the transverse plane which is mostly captured by the linear spin wave theory, though a renormalization of the magnon dispersion is observed at higher energy which may be due to the interactions between the single quasiparticles. With the same impurity density level, the lowest two magnon bands split near the K points as shown in Fig. 3(e).

To further study the impurity effect of high symmetry points we obtain the $\chi(\mathbf{q}, \omega)$ near the M points. As shown in Fig. 4(a), in the "Y" supersolid state the ro-
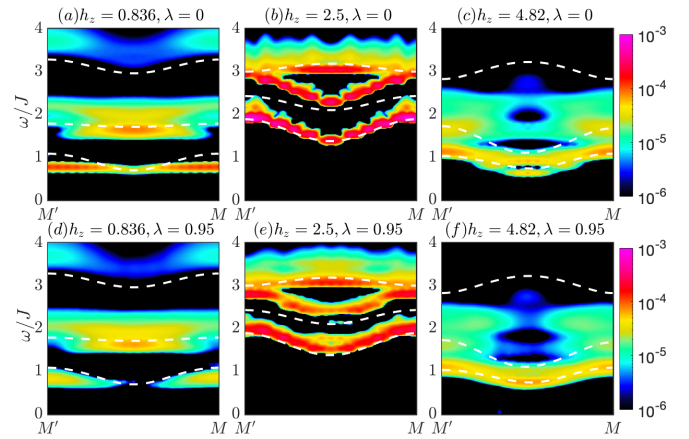

FIG. 4. The dynamical structure factor near M points. Panel (a) and (d) are obtained in the "Y" supersolid phase. Panel (b) and (e) are obtained in the UUD phase. Panel (c) and (f) are obtained in the "V" supersolid phase. Panel (a), (b), and (c) are obtained without the impurities, while panel (d), (e), and (f) are obtained with the impurities. The white dashed lines represent the linear spin wave results; see more details in the Supplemental Material [56].

tonlike minimum at the M points is found to be almost flat in the spectral weight, which is consistent with previous study using the infinite projected entangled-pair state (iPEPS) methods [31]. The flatness is not observed in the linear spin wave dispersion, and is caused by the interactions between the single magnon branches. However, the excitation energy at the M points is closer to the linear spin wave results in this easy-axis Heisenberg model, as compared to the near isotropic one [76, 78]. With impurities, the spectral weight at the M points broaden as shown in Fig. 4(d), which may decay into higher energy modes due to the impurity. Similar broadening effect induced by the impurity can be found in the "V" supersolid state, as shown in Figs. 4(c) and (f). Except for the broadening effect, the $\chi(\mathbf{q}, \omega)$ remains almost unchanged in the presence of impurity. On the other hand, a band splitting is identified at the lowest energy in the UUD state with impurity, which can be seen by comparing Figs. 4(b) and (d).

Summary.— Through extensive numerical simulations on width-6 cylinders, we have investigated the dynamical spin structure factors in various magnetic field-induced states in the easy-axis triangular-lattice Heisenberg antiferromagnets. In particular, we develop a numerical characterization of the dissipationless dynamics in the spin supersolid state through the excitation spectrum with impurities. We show a robust gapless Goldstone mode at the K points against finite impurities in the spin supersolid states, which provides direct evidence for the spin superfluidity that can be observed in neutron scattering experiments. By contrast, for the UUD state we find that the lower bands split at the same impurity density. For

the spectral weight at higher energies such as the roton-like minimum, the impurities cause a broadening effect, while the overall profile of the spectrum remains almost unchanged. We believe that our results could also be applied to other spin supersolid candidate materials, such as $K_2Co(SeO_3)_2$ [79–84] and $Na_2BaNi(PO_4)_2$ [85–87] as long as the gapless Goldstone mode can be observed.

In addition, we study the superfluid density of various states at both zero and finite temperatures, which is characterized by the superfluid stiffness through a π-phase twist. We find a finite superfluid stiffness in both "Y" and "V" supersolid states, suggesting that dissipationless dynamics from spin supercurrent may persist up to $T/J \approx 0.1$, which is consistent with the spin Seebeck effect calculations [55].

[1] A. J. Leggett, Can a solid be "superfluid"?, Physical Review Letters **25**, 1543 (1970).

[2] G. Chester, Speculations on Bose-Einstein condensation and quantum crystals, Physical Review A **2**, 256 (1970).

[3] E. Kim and M. H.-W. Chan, Probable observation of a supersolid helium phase, Nature **427**, 225 (2004).

[4] S. Balibar, The enigma of supersolidity, Nature **464**, 176 (2010).

[5] M. H.-W. Chan, R. Hallock, and L. Reatto, Overview on solid ^{4}He and the issue of supersolidity, Journal of Low Temperature Physics **172**, 317 (2013).

[6] L. Tanzi, E. Lucioni, F. Famà, J. Catani, A. Fioretti, C. Gabbanini, R. N. Bisset, L. Santos, and G. Modugno, Observation of a dipolar quantum gas with metastable supersolid properties, Physical Review Letters **122**, 130405 (2019).

[7] F. Böttcher, J.-N. Schmidt, M. Wenzel, J. Hertkorn, M. Guo, T. Langen, and T. Pfau, Transient supersolid properties in an array of dipolar quantum droplets, Physical Review X **9**, 011051 (2019).

[8] L. Chomaz, D. Petter, P. Ilzhöfer, G. Natale, A. Trautmann, C. Politi, G. Durastante, R. Van Bijnen, A. Patscheider, M. Sohmen, *et al.*, Long-lived and transient supersolid behaviors in dipolar quantum gases, Physical Review X **9**, 021012 (2019).

[9] M. Guo, F. Böttcher, J. Hertkorn, J.-N. Schmidt, M. Wenzel, H. P. Büchler, T. Langen, and T. Pfau, The low-energy goldstone mode in a trapped dipolar supersolid, Nature **574**, 386 (2019).

[10] L. Tanzi, S. Roccuzzo, E. Lucioni, F. Famà, A. Fioretti, C. Gabbanini, G. Modugno, A. Recati, and S. Stringari, Supersolid symmetry breaking from compressional oscillations in a dipolar quantum gas, Nature **574**, 382 (2019).

[11] G. Natale, R. van Bijnen, A. Patscheider, D. Petter, M. J. Mark, L. Chomaz, and F. Ferlaino, Excitation spectrum of a trapped dipolar supersolid and its experimental evidence, Physical Review Letters **123**, 050402 (2019).

[12] L. Tanzi, J. Maloberti, G. Biagioni, A. Fioretti, C. Gabbanini, and G. Modugno, Evidence of superfluidity in a dipolar supersolid from nonclassical rotational inertia, Science **371**, 1162 (2021).

[13] M. A. Norcia, E. Poli, C. Politi, L. Klaus, T. Bland, M. J. Mark, L. Santos, R. N. Bisset, and F. Ferlaino, Can angular oscillations probe superfluidity in dipolar supersolids?, Physical Review Letters **129**, 040403 (2022).

[14] A. Recati and S. Stringari, Supersolidity in ultracold dipolar gases, Nature Reviews Physics **5**, 735 (2023).

[15] M. Šindik, T. Zawiślak, A. Recati, and S. Stringari, Sound, superfluidity, and layer compressibility in a ring dipolar supersolid, Physical Review Letters **132**, 146001 (2024).

[16] G. Bougas, T. Bland, H. Sadeghpour, and S. Mistakidis, Signatures of rigidity and second sound in dipolar supersolids, arXiv preprint arXiv:2506.22290 (2025).

[17] S. Wessel and M. Troyer, Supersolid hard-core bosons on the triangular lattice, Physical Review Letters **95**, 127205 (2005).

[18] D. Heidarian and K. Damle, Persistent supersolid phase of hard-core bosons on the triangular lattice, Physical Review Letters **95**, 127206 (2005).

[19] R. Melko, A. Paramekanti, A. Burkov, A. Vishwanath, D. Sheng, and L. Balents, Supersolid order from disorder: Hard-core bosons on the triangular lattice, Physical Review Letters **95**, 127207 (2005).

[20] A. Burkov and L. Balents, Superfluid-insulator transitions on the triangular lattice, Physical Review B—Condensed Matter and Materials Physics **72**, 134502 (2005).

[21] M. Boninsegni and N. Prokof'ev, Supersolid phase of hard-core bosons on a triangular lattice, Physical Review Letters **95**, 237204 (2005).

[22] R. G. Melko, A. Del Maestro, and A. Burkov, Striped supersolid phase and the search for deconfined quantum criticality in hard-core bosons on the triangular lattice, Physical Review B—Condensed Matter and Materials Physics **74**, 214517 (2006).

[23] J.-Y. Gan, Y.-C. Wen, and Y. Yu, Supersolidity and phase diagram of soft-core bosons on a triangular lattice, Physical Review B—Condensed Matter and Materials Physics **75**, 094501 (2007).

[24] A. Sen, P. Dutt, K. Damle, and R. Moessner, Variational wave-function study of the triangular lattice supersolid, Physical Review Letters **100**, 147204 (2008).

[25] F. Wang, F. Pollmann, and A. Vishwanath, Extended supersolid phase of frustrated hard-core bosons on a triangular lattice, Physical Review Letters **102**, 017203 (2009).

[26] H. Jiang, M. Weng, Z. Weng, D. Sheng, and L. Balents, Supersolid order of frustrated hard-core bosons in a triangular lattice system, Physical Review B—Condensed Matter and Materials Physics **79**, 020409 (2009).

[27] X.-F. Zhang, R. Dillenschneider, Y. Yu, and S. Eggert, Supersolid phase transitions for hard-core bosons on a triangular lattice, Physical Review B—Condensed Matter and Materials Physics **84**, 174515 (2011).

[28] H.-C. Jiang, L. Fu, and C. Xu, Pair superfluid and supersolid of correlated hard-core bosons on a triangular lattice, Physical Review B—Condensed Matter and Materials Physics **86**, 045129 (2012).

[29] D. Yamamoto, G. Marmorini, and I. Danshita, Quantum phase diagram of the triangular-lattice XXZ model in a magnetic field, Physical Review Letters **112**, 127203 (2014).

[30] D. Sellmann, X.-F. Zhang, and S. Eggert, Phase diagram of the antiferromagnetic XXZ model on the triangular lattice, Physical Review B **91**, 081104 (2015).

[31] R. Chi, J. Hu, H.-J. Liao, and T. Xiang, Dynamical spectra of spin supersolid states in triangular antiferromagnets, Physical Review B **110**, L180404 (2024).

[32] Y. Gao, Y.-C. Fan, H. Li, F. Yang, X.-T. Zeng, X.-L. Sheng, R. Zhong, Y. Qi, Y. Wan, and W. Li, Spin supersolidity in nearly ideal easy-axis triangular quantum antiferromagnet $Na_2BaCo(PO_4)_2$, npj Quantum Materials **7**, 89 (2022).

[33] R. Zhong, S. Guo, G. Xu, Z. Xu, and R. J. Cava, Strong quantum fluctuations in a quantum spin liquid candidate with a Co-based triangular lattice, Proceedings of the National Academy of Sciences **116**, 14505 (2019).

[34] N. Li, Q. Huang, X. Yue, W. Chu, Q. Chen, E. Choi, X. Zhao, H. Zhou, and X. Sun, Possible itinerant excitations and quantum spin state transitions in the effective spin-1/2 triangular-lattice antiferromagnet $Na_2BaCo(PO_4)_2$, Nature Communications **11**, 4216 (2020).

[35] S. Lee, C. Lee, A. Berlie, A. Hillier, D. T. Adroja, R. Zhong, R. Cava, Z. Jang, and K.-Y. Choi, Temporal and field evolution of spin excitations in the disorder-free triangular antiferromagnet $Na_2BaCo(PO_4)_2$, Physical Review B **103**, 024413 (2021).

[36] C. Wellm, W. Roscher, J. Zeisner, A. Alfonsov, R. Zhong, R. J. Cava, A. Savoyant, R. Hayn, J. van den Brink, B. Büchner, *et al.*, Frustration enhanced by Kitaev exchange in a $\tilde{j}_{eff} = \frac{1}{2}$ triangular antiferromagnet, Physical Review B **104**, L100420 (2021).

[37] Y. Huang, D. Dai, C. Zhao, J. Ni, L. Wang, B. Pan, B. Gao, P. Dai, and S. Li, Thermal conductivity of triangular-lattice antiferromagnet $Na_2BaCo(PO_4)_2$: absence of itinerant fermionic excitations, arXiv preprint arXiv:2206.08866 (2022).

[38] X.-Y. Liu, Y. Gao, H. Li, W. Jin, J. Xiang, H. Jin, Z. Chen, W. Li, and G. Su, Quantum spin liquid candidate as superior refrigerant in cascade demagnetization cooling, Communications Physics **5**, 233 (2022).

[39] J. Sheng, L. Wang, A. Candini, W. Jiang, L. Huang, B. Xi, J. Zhao, H. Ge, N. Zhao, Y. Fu, *et al.*, Two-dimensional quantum universality in the spin-1/2 triangular-lattice quantum antiferromagnet $Na_2BaCo(PO_4)_2$, Proceedings of the National Academy of Sciences **119**, e2211193119 (2022).

[40] J. Xiang, C. Zhang, Y. Gao, W. Schmidt, K. Schmalzl, C.-W. Wang, B. Li, N. Xi, X.-Y. Liu, H. Jin, *et al.*, Giant magnetocaloric effect in spin supersolid candidate $Na_2BaCo(PO_4)_2$, Nature **625**, 270 (2024).

[41] Y. Gao, C. Zhang, J. Xiang, D. Yu, X. Lu, P. Sun, W. Jin, G. Su, and W. Li, Double magnon-roton excitations in the triangular-lattice spin supersolid, Physical Review B **110**, 214408 (2024).

[42] D. Zhang, Y. Zhu, G. Zheng, K.-W. Chen, Q. Huang, L. Zhou, Y. Liu, K. Jenkins, A. Chan, H. Zhou,

[43] *et al.*, Field tunable BKT and quantum phase transitions in spin-1/2 triangular lattice antiferromagnet, arXiv preprint arXiv:2411.04755 (2024).

[43] G. Hussain, J. Zhang, M. Zhang, L. Yadav, Y. Ding, C. Zheng, S. Haravifard, and X. Wang, Experimental evidence of crystal-field, Zeeman-splitting, and spin-phonon excitations in the quantum supersolid $Na_2BaCo(PO_4)_2$, Physical Review B **111**, 155129 (2025).

[44] T. Popescu, N. Gora, F. Demmel, Z. Xu, R. Zhong, T. Williams, R. Cava, G. Xu, and C. Stock, Zeeman split Kramers doublets in spin-supersolid candidate $Na_2BaCo(PO_4)_2$, Physical Review Letters **134**, 136703 (2025).

[45] X. Xu, Z. Wu, Y. Chen, Q. Huang, Z. Hu, X. Shi, K. Du, S. Li, R. Bian, R. Yu, *et al.*, NMR study of supersolid phases in the triangular-lattice antiferromagnet $Na_2BaCo(PO_4)_2$, arXiv preprint arXiv:2504.08570 (2025).

[46] L. Woodland, R. Okuma, J. R. Stewart, C. Balz, and R. Coldea, From continuum excitations to sharp magnons via transverse magnetic field in the spin-1/2 Ising-like triangular lattice antiferromagnet $Na_2BaCo(PO_4)_2$, Physical Review B **112**, 104413 (2025).

[47] J. Sheng, L. Wang, W. Jiang, H. Ge, N. Zhao, T. Li, M. Kofu, D. Yu, W. Zhu, J.-W. Mei, *et al.*, Continuum of spin excitations in an ordered magnet, The Innovation (2025).

[48] J. Xiang, E. Lv, Q. Shen, C. Su, X. He, Y. Zhu, Y. Gao, X.-Y. Liu, D.-W. Qu, X. Wang, X. Chen, Q. Zhao, H. Li, S. Li, J. Yang, J. Luo, P. Sun, W. Jin, Y. Qi, R. Zhou, W. Li, and G. Su, Universal magnetocaloric effect near quantum critical point of magnon bose-einstein condensation (2025), arXiv:2508.05750 [cond-mat.str-el].

[49] M. Drescher, L. Vanderstraeten, R. Moessner, and F. Pollmann, Dynamical signatures of symmetry-broken and liquid phases in an $S = \frac{1}{2}$ heisenberg antiferromagnet on the triangular lattice, Physical Review B **108**, L220401 (2023).

[50] M. Drescher, L. Vanderstraeten, R. Moessner, and F. Pollmann, Spectral functions of an extended antiferromagnetic $S = 1/2$ Heisenberg model on the triangular lattice (2025), arXiv:2508.17292 [cond-mat.str-el].

[51] H. Jia, B. Ma, Z. Wang, and G. Chen, Quantum spin supersolid as a precursory Dirac spin liquid in a triangular lattice antiferromagnet, Physical Review Research **6**, 033031 (2024).

[52] S. Takei and Y. Tserkovnyak, Superfluid spin transport through easy-plane ferromagnetic insulators, Physical Review Letters **112**, 227201 (2014).

[53] A. Qaiumzadeh, H. Skarsvåg, C. Holmqvist, and A. Brataas, Spin superfluidity in biaxial antiferromagnetic insulators, Physical Review Letters **118**, 137201 (2017).

[54] W. Yuan, Q. Zhu, T. Su, Y. Yao, W. Xing, Y. Chen, Y. Ma, X. Lin, J. Shi, R. Shindou, *et al.*, Experimental signatures of spin superfluid ground state in canted antiferromagnet Cr_2O_3 via nonlocal spin transport, Science Advances **4**, eaat1098 (2018).

[55] Y. Gao, Y. Huang, S. Maekawa, and W. Li, Spin Seebeck effect of triangular-lattice spin supersolid, arXiv preprint arXiv:2506.22414 (2025).

[56] See Supplemental Material for more detailed results.

[57] S. R. White, Density matrix formulation for quantum renormalization groups, Physical Review Letters **69**,

2863 (1992).

[58] S. R. White, Density-matrix algorithms for quantum renormalization groups, Physical Review B **48**, 10345 (1993).

[59] U. Schollwöck, The density-matrix renormalization group in the age of matrix product states, Annals of physics **326**, 96 (2011).

[60] J. Haegeman, J. I. Cirac, T. J. Osborne, I. Pižorn, H. Verschelde, and F. Verstraete, Time-dependent variational principle for quantum lattices, Physical Review letters **107**, 070601 (2011).

[61] J. Haegeman, C. Lubich, I. Oseledets, B. Vandereycken, and F. Verstraete, Unifying time evolution and optimization with matrix product states, Physical Review B **94**, 165116 (2016).

[62] Q. Li, Y. Gao, Y.-Y. He, Y. Qi, B.-B. Chen, and W. Li, Tangent space approach for thermal tensor network simulations of the 2D Hubbard model, Physical Review Letters **130**, 226502 (2023).

[63] M. Yang and S. R. White, Time-dependent variational principle with ancillary Krylov subspace, Physical Review B **102**, 094315 (2020).

[64] B.-B. Chen, L. Chen, Z. Chen, W. Li, and A. Weichselbaum, Exponential thermal tensor network approach for quantum lattice models, Phys. Rev. X **8**, 031082 (2018).

[65] B.-B. Chen, Y.-J. Liu, Z. Chen, and W. Li, Series-expansion thermal tensor network approach for quantum lattice models, Phys. Rev. B **95**, 161104 (2017).

[66] A. Gleis, J.-W. Li, and J. von Delft, Controlled bond expansion for density matrix renormalization group ground state search at single-site costs, Phys. Rev. Lett. **130**, 246402 (2023).

[67] J.-W. Li, A. Gleis, and J. von Delft, Time-dependent variational principle with controlled bond expansion for matrix product states, Phys. Rev. Lett. **133**, 026401 (2024).

[68] P. C. Canfield, New materials physics, Reports on Progress in Physics **83**, 016501 (2019).

[69] J. Schmidt, A. Sapkota, C. L. Mueller, S. Xiao, S. Huyan, T. J. Slade, R. Ribeiro, S.-W. Lee, S. Bud'ko, and P. Canfield, Tuning the structure and superconductivity of $SrNi_2P_2$ by Rh substitution, Physical Review B **111**, 054102 (2025).

[70] J. Karpinski, N. D. Zhigadlo, S. Katrych, R. Puzniak, K. Rogacki, and R. Gonnelli, Single crystals of MgB_2: Synthesis, substitutions and properties, Physica C: Superconductivity **456**, 3 (2007).

[71] J. Langmann, H. Kepenci, G. Eickerling, K. Batke, A. Jesche, M. Xu, P. Canfield, and W. Scherer, Experimental X-ray charge-density studies- a suitable probe for superconductivity? a case study on MgB_2, The Journal of Physical Chemistry A **126**, 8494 (2022).

[72] C. Adriano, M. Xu, S. Huyan, K. R. Pakuszewski, A. P. Machado, B. Schrunk, S. L. Bud'ko, R. A. Ribeiro, P. C. Canfield, and A. Kaminski, Tuning the electronic properties of MgB_2 by substitution with Mn and C, Journal of Physics: Condensed Matter (2025).

[73] X.-F. Zhang, Y.-C. Wen, and S. Eggert, Static impurities in a supersolid of interacting hard-core bosons on a triangular lattice, Physical Review B—Condensed Matter and Materials Physics **82**, 220501 (2010).

[74] T. Holstein and H. Primakoff, Field dependence of the intrinsic domain magnetization of a ferromagnet, Physical Review **58**, 1098 (1940).

[75] F. Ferrari and F. Becca, Dynamical structure factor of the J_1-J_2 heisenberg model on the triangular lattice: magnons, spinons, and gauge fields, Physical Review X **9**, 031026 (2019).

[76] R. Chi, Y. Liu, Y. Wan, H.-J. Liao, and T. Xiang, Spin excitation spectra of anisotropic spin-1/2 triangular lattice heisenberg antiferromagnets, Physical Review Letters **129**, 227201 (2022).

[77] J. G. Rau, P. A. McClarty, and R. Moessner, Pseudo-goldstone gaps and order-by-quantum disorder in frustrated magnets, Physical Review Letters **121**, 237201 (2018).

[78] S. Ito, N. Kurita, H. Tanaka, S. Ohira-Kawamura, K. Nakajima, S. Itoh, K. Kuwahara, and K. Kakurai, Structure of the magnetic excitations in the spin-1/2 triangular-lattice Heisenberg antiferromagnet $Ba_3CoSb_2O_9$, Nature Communications **8**, 235 (2017).

[79] R. Zhong, S. Guo, and R. Cava, Frustrated magnetism in the layered triangular lattice materials $K_2Co(SeO_3)_2$ and $Rb_2Co(SeO_3)_2$, Physical Review Materials **4**, 084406 (2020).

[80] T. Chen, A. Ghasemi, J. Zhang, L. Shi, Z. Tagay, L. Chen, E.-S. Choi, M. Jaime, M. Lee, Y. Hao, *et al.*, Phase diagram and spectroscopic evidence of supersolids in quantum ising magnet $K_2Co(SeO_3)_2$, arXiv e-prints , arXiv (2024).

[81] M. Zhu, V. Romerio, N. Steiger, S. Nabi, N. Murai, S. Ohira-Kawamura, K. Y. Povarov, Y. Skourski, R. Sibille, L. Keller, *et al.*, Continuum excitations in a spin supersolid on a triangular lattice, Physical Review Letters **133**, 186704 (2024).

[82] Y. Xu, J. Hasik, B. Ponsioen, and A. H. Nevidomskyy, Simulating spin dynamics of supersolid states in a quantum Ising magnet, Physical Review B **111**, L060402 (2025).

[83] M. Ulaga, J. Kokalj, T. Tohyama, and P. Prelovšek, Easy-axis heisenberg model on the triangular lattice: From a supersolid to a gapped solid, Physical Review B **111**, 174442 (2025).

[84] M. Zhu, L. M. Chinellato, V. Romerio, N. Murai, S. Ohira-Kawamura, C. Balz, Z. Yan, S. Gvasaliya, Y. Kato, C. D. Batista, and A. Zheludev, Wannier states and spin supersolid physics in the triangular antiferromagnet $K_2Co(SeO_3)_2$, npj Quantum Materials **10**, 74 (2025).

[85] J. Sheng, J.-W. Mei, L. Wang, X. Xu, W. Jiang, L. Xu, H. Ge, N. Zhao, T. Li, A. Candini, *et al.*, Bose–einstein condensation of a two-magnon bound state in a spin-1 triangular lattice, Nature Materials , 1 (2025).

[86] J. Sheng, J. Hu, L. Xu, L. Wang, X. Shi, R. Chi, D. Yu, A. Podlesnyak, P. Piyawongwatthana, N. Murai, *et al.*, Unveiling the quadrupole waves in spin nematics, arXiv preprint arXiv:2503.13888 (2025).

[87] Q. Huang, H. Zhang, Y. Hao, W. Yao, D. M. Pajerowski, A. A. Aczel, E. S. Choi, K. Barros, B. Normand, H. Zhou, *et al.*, Universal dynamics of a pair condensate, arXiv preprint arXiv:2503.13609 (2025).

[88] M. Fishman, S. R. White, and E. M. Stoudenmire, The ITensor Software Library for Tensor Network Calculations, SciPost Phys. Codebases , 4 (2022).

[89] R. Verresen, R. Moessner, and F. Pollmann, Avoided quasiparticle decay from strong quantum interactions, Nature Physics **15**, 750 (2019).

[90] R. Smit, S. Keupert, O. Tsyplyatyev, P. Maksimov, A. L.

Chernyshev, and P. Kopietz, Magnon damping in the zigzag phase of the Kitaev-Heisenberg-γ model on a honeycomb lattice, Physical Review B **101**, 054424 (2020).

[91] J. Colpa, Diagonalization of the quadratic boson Hamiltonian, Physica A: Statistical Mechanics and its Applications **93**, 327 (1978).

[92] O. Maldonado, On the Bogoliubov transformation for quadratic boson observables, Journal of Mathematical Physics **34**, 5016 (1993).

[93] A. Serga, C. Sandweg, V. Vasyuchka, M. Jungfleisch, B. Hillebrands, A. Kreisel, P. Kopietz, and M. Kostylev, Brillouin light scattering spectroscopy of parametrically excited dipole-exchange magnons, Physical Review B—Condensed Matter and Materials Physics **86**, 134403 (2012).

Supplemental Material for "Dissipationless dynamics of spin supersolid states in a spin-1/2 triangular antiferromagnet with impurities"

In the Supplemental Material, we provide more numerical results to support the main text. In Sec. I, we discuss more details of the numerical methods and evaluate the convergence of the dynamical spin structure factor. In Sec. II, we show more details of the impurity distribution in real space. In Sec. III, we present more results of the dynamical spin structure factor at other symmetry points and lower impurity densities. In Sec. IV, we present more data on the superfluid stiffness, $\langle m_z^2 \rangle$ and $\langle m_\perp^2 \rangle$ for various lattice sizes and impurities. In Sec. V, we discuss the details of the linear spin wave theory.

I.   NUMERICAL ALGORITHM AND CONVERGENCE

The time-dependent variational principle (TDVP) methods are used for real-time evolutions of the ground state. The time that can be faithfully accessed during numerical calculation is limited by the bond dimensions, because of the entanglement entropy growth during time evolution. We use bond dimensions up to $D = 2200$ for the time up to $\tau_{tot} = 50/J$, and the time correlator is measured at every $\delta\tau = 0.5/J$.

For finite temperature calculations, the procedure starts from a high-temperature expansion of the density matrix $\rho(\beta_0) \simeq 1 - \beta_0 H + \frac{\beta_0^2}{2}H^2$ [62, 65], with $\beta_0 = 2^{-15}$. We then successively double the inverse temperature until $\beta = 1$, followed by a linear evolution in β with step size $\delta\beta = 1$ down to the lowest temperature. In practice, we employ the one-site tangent space tensor renormalization group scheme with U(1) symmetry on the $N = 18 \times 6$ lattice with bond dimensions up to $D = 2000$. The bond dimension is enlarged through the controlled bond expansion algorithm [66, 67], with an increment of $\delta D = 200$ and a truncation error maintained at $\epsilon \lesssim 5 \times 10^{-5}$.

The dynamical spin structure factor is calculated from the time dependent spin correlations as given by the Eq. 4 in the main text. Due to limited simulation time, we apply a smearing factor of $e^{-\eta\tau}$ to the time series before performing the discrete Fourier transformation where $\eta = 1/\tau_{tot}$ and τ_{tot} is the total simulation time. To evaluate the convergence of the dynamical spin structure factor, we compare the simulations with different maximum bond dimensions. For a direct comparison we use the same τ_{tot} for the calculation with different maximum bond dimensions. Comparing Figs. S1 (a) and (c) with Figs. S1(b) and (d) as an example, the dynamical spin structure factor with bond dimensions up to $D = 2200$ is almost the same as the one with up to $D = 1400$. This is mainly because large bond dimensions are only needed at the later time where the entanglement entropy increases, while the convolution with the smearing factor has distributed the main weight to the simulation data at the early time.

II.   IMPURITY DISTRIBUTION

The impurities are placed evenly in the bulk of the lattice as shown in Figs. S2(a), (b), and (c) for the "Y" supersolid state, the up-up-down (UUD) state, and the "V" supersolid state, respectively. The four impurities in the summation of the bulk $N_{mid} = \frac{3}{4}L_x \times L_y$ sites correspond to an impurity density level of 1.85%. For simplicity, we only consider the impurity on the same sublattice where the same magnetic structure in z direction is pinned by the impurities. In this case, the $\langle m_z^2 \rangle$ remains almost unchanged. For a general impurity configuration where impurities are placed randomly on the three different sublattices, the interference of impurities may reduce the $\langle m_z^2 \rangle$ but the impact to superfluid stiffness remains similar [73].

III.   ADDITION RESULTS OF THE DYNAMICAL STRUCTURE FACTOR

As suggested by the study of the easy-axis anisotropic Heisenberg model on the triangular lattice [89], the rotonlike minimum might also appear at the Y_1 points. Here we keep the same impurity density level of 1.85% and other parameters as the Figs. 3 and 4 in the main text. For the "Y" supersolid state with impurities, we use a shorter $\tau_{tot} = 42/J$ for better numerical convergence. Figure S3 shows the $\chi(\mathbf{q}, \omega)$ at the Y_1 points between the A and B points for various states. As shown in Figs. S3(a) and (d), we identify a rotonlike minimum in the "Y" supersolid state which remains almost the same in the presence of impurities. This minimum at the Y_1 points is clearly visible as compared to the state without magnetic field [49], and cannot be captured by the linear spin wave theory as magnon dispersions are strongly renormalized. In the "V" supersolid state the rotonlike minimum at the Y_1 points disappears,
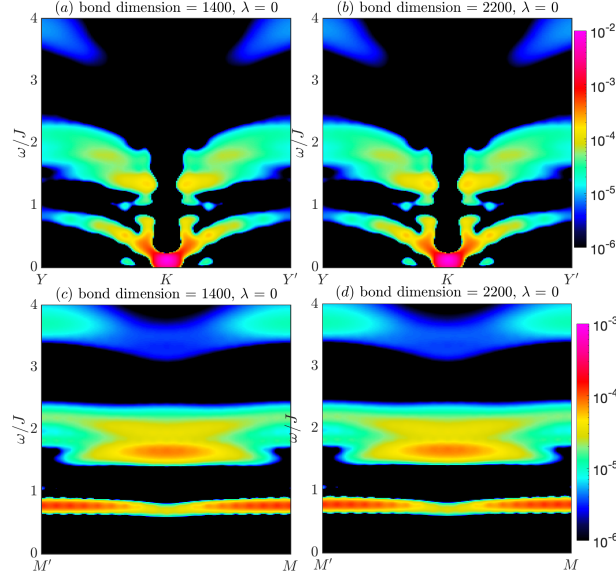
FIG. S1. The dynamical structure factor obtained with different bond dimensions for the "Y" supersolid state at $h_z/J = 0.836$ on the $L_x \times L_y = 48 \times 6$ lattice. Panels (a) and (b) show the dynamical structure factor near K points, Panels (c) and (d) show the dynamical structure factor near M points. Panels (a) and (c) are obtained with $D = 1400$, Panels (b) and (d) are obtained with $D = 2200$.
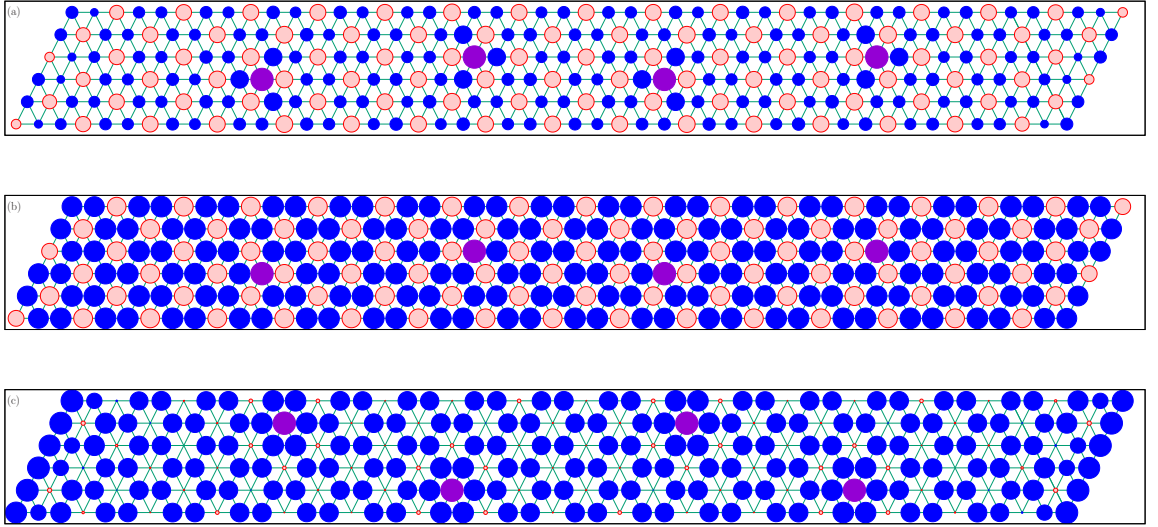

FIG. S2. The $\langle S_i^z \rangle$ in real space for the ground state with impurities for (a) the "Y" supersolid state at $h_z/J = 0.836$, (b) the up-up-down state at $h_z/J = 2.5$, and (c) the "V" supersolid state at $h_z/J = 4.82$. The results are obtained on the $N = 48 \times 6$ lattice with $\lambda = 0.95$. The blue solid circles represent positive spin values, and the red shaded circles represent negative spin values. The purple solid circles represent the impurity sites with a positive spin value. The radius represents the magnitude where the purple ones have $\langle S_i^z \rangle \approx 0.5$.

as shown in Figs. S3(c) and (f), and the lowest energy excitations can be qualitatively reproduced by the linear spin wave results. For the spin supersolid states, the whole spectrum remains similar with impurities except for some broadening of the spectral weight. However, the splitting of the lowest band at B points in the UUD state due to impurities can be seen by comparing Figs. S3(b) and (e).

We also show the effect of a smaller impurity density level on the dynamical spin structure factor in the UUD state.
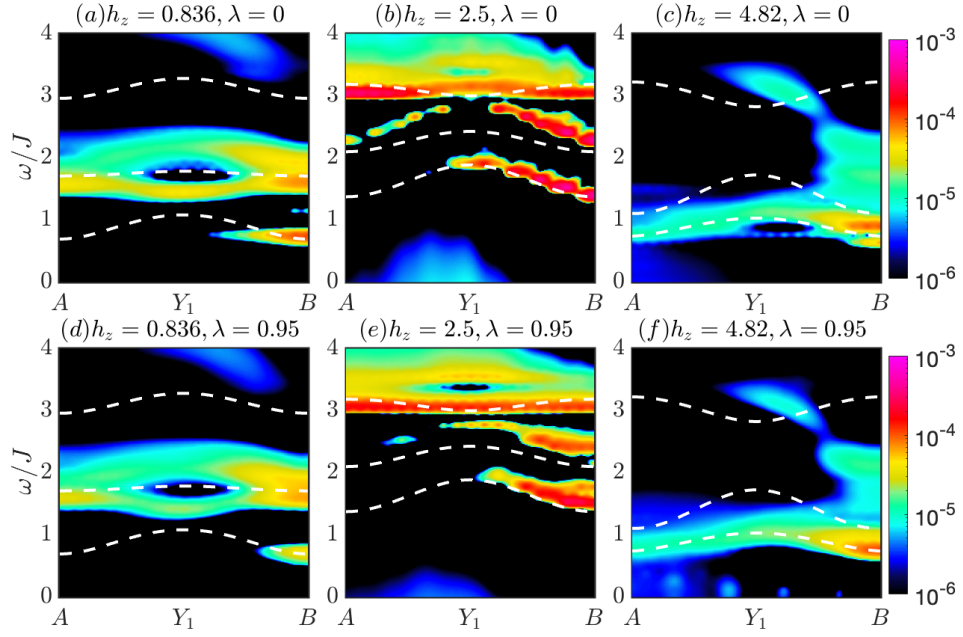
FIG. S3. The dynamical structure factor near Y_1 points. Panel (a) and (d) are obtained in the "Y" supersolid phase. Panel (b) and (e) are obtained in the UUD phase. Panel (c) and (f) are obtained in the "V" supersolid phase. Panel (a), (b), and (c) are obtained without the impurities, while panel (d), (e), and (f) are obtained with the impurities. The white dashed lines represent the linear spin wave results.
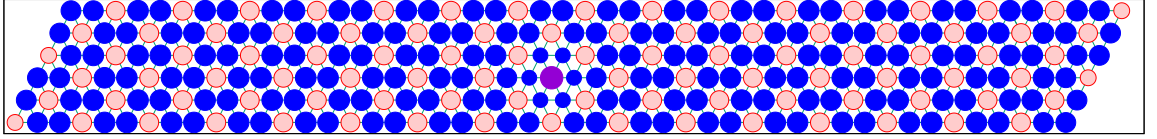

FIG. S4. The $\langle S_i^z \rangle$ in real space for the ground state with one impurity on the $N = 48 \times 6$ lattice for the up-up-down state at $h_z/J = 2.5$ and $\lambda = 0.9$. The blue solid circles represent positive spin values, and the red shaded circles represent negative spin values. The purple solid circles represent the impurity sites with a positive spin value. The radius represents the magnitude where the purple ones have $\langle S_i^z \rangle \approx 0.5$.

As shown in Fig. S4, a single impurity is placed in the middle of the lattice. The summation of $\sum_{i,j}$ is between $L_x = 18$ and $L_x = 30$, which corresponds to the impurity density of 1.28%. The dynamical spin structure factor along different paths in the Brillouin zone is shown in Fig. S5, where the bands start to split at the K points while other bands remain almost the same.
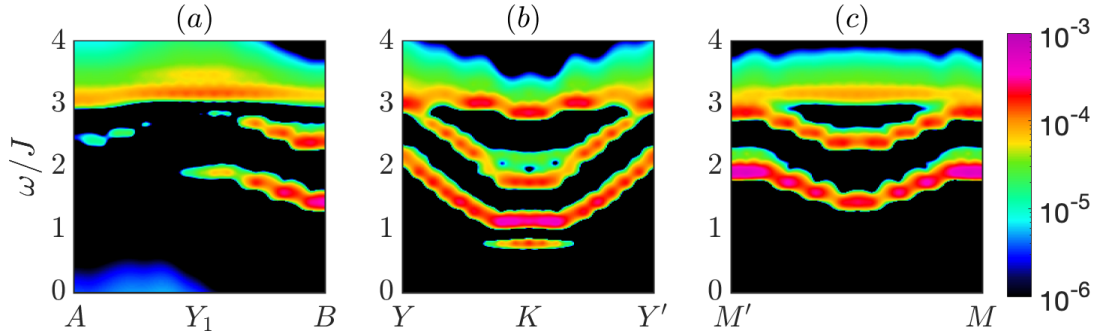

FIG. S5. The dynamical structure factor are obtained with impurity density of 1.28% in the UUD state for $h_z/J = 2.5, \lambda = 0.9$.
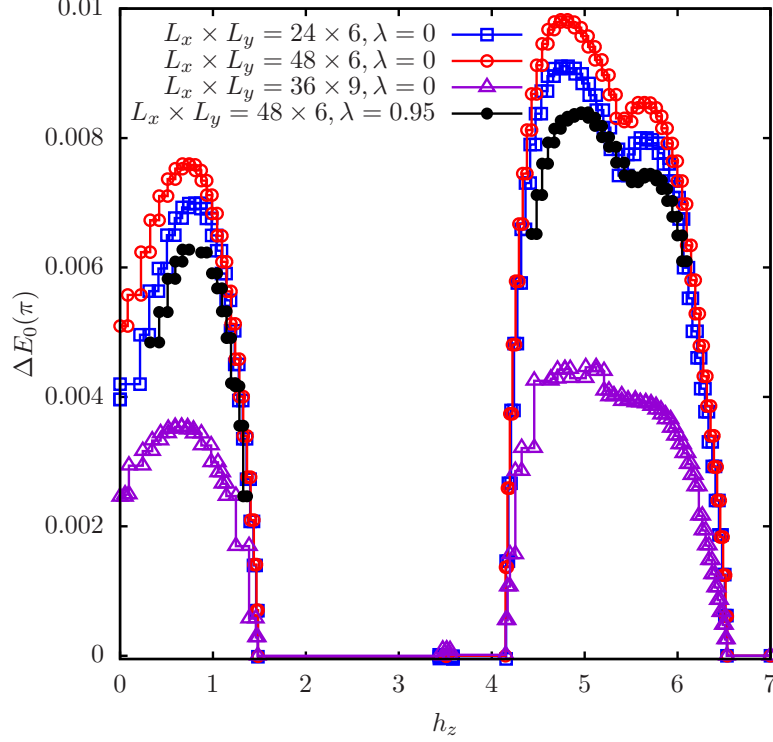
FIG. S6. The $\Delta E_0(\pi)$ obtained for various h_z without impurity on lattices of $L_x \times L_y = 24 \times 6$, 48×6 and 36×9, and with finite impurities on the lattice of $L_x \times L_y = 48 \times 6$. A few data in the "Y" supersolid state with impurites is ignored because the impurities cause a domain wall in the magnetic structure in z direction that might lead to a higher energy, which is beyond the scope of current study.

IV. ADDITIONAL RESULTS OF THE SUPERFLUID STIFFNESS, $\langle m_z^2 \rangle$ AND $\langle m_\perp^2 \rangle$

Although the superfluid stiffness is defined in the limit of $\theta \to 0$, we are restricted by the finite numerical accuracy of the ground state energy and the free energy. In practice, we choose $\theta = \pi$ where the energy difference is much larger than the numerical truncation error. A small θ would lead to a large variance especially for the results in the high field limit. To test the finite size effect of our results, we obtain the $\Delta E_0(\pi)$ on lattices with different L_x and L_y. In the UUD state we notice an edge excitation induced by the twisted phase $\theta = \pi$. Thus, the ground state energy is obtained by averaging over the bulk of the lattice. As shown in Fig. S6, while keeping the same $L_y = 6$ the $\Delta E_0(\pi)$ becomes slightly larger for larger L_x. However, when both L_x and L_y increase proportionally, $\Delta E_0(\pi)$ decreases. Previous papers have shown that the $\Delta E_0(\pi)$ remains finite after the finite size scaling in the zero magnetic field [26]. For finite fields, future study on larger systems may be needed to determine the $\Delta E_0(\pi)$ in the thermodynamic limit. Although our results are based on finite-size quasi-one dimensional cylindrical geometry, the method of identifying superfluidity through the dynamical structure factor with impurity is robust and could be tested in experiments.

When impurity density increases to 1.85%, the superfluid stiffness slightly decreases but remains finite. For the "Y" and "V" supersolid states, we show the $\Delta E_0(\pi)$ without impurities and with impurity density of 1.85% in Fig. S6 which is obtained on the same lattice of $L_y \times L_x = 48 \times 6$. In the presence of impurities, the $\Delta E_0(\pi)$ becomes consistently lower.

In addition, we have obtained the $\langle m_z^2 \rangle$ and $\langle m_\perp^2 \rangle$ for different phases on various lattices. As shown in Fig. S7, the $\langle m_z^2 \rangle = S^z(\mathbf{K})/L_y^2 = \frac{1}{L_y^4} \sum_{i,j} e^{i\mathbf{K} \cdot (\mathbf{r}_i - \mathbf{r}_j)} \langle S_i^z S_j^z \rangle$ remains robust with various L_x and L_y, while the $\langle m_\perp^2 \rangle = S^{xy}(\mathbf{K})/L_y^2 = \frac{1}{L_y^4} \sum_{i,j} e^{i\mathbf{K} \cdot (\mathbf{r}_i - \mathbf{r}_j)} \langle S_i^x S_j^x + S_i^y S_j^y \rangle$ becomes smaller on a larger system of $L_x \times L_y = 36 \times 9$, which is consistent with the results of superfluid stiffness on the larger system in Fig. S6. For the UUD state, the $\langle m_\perp^2 \rangle$ also becomes smaller on the larger lattice of $L_x \times L_y = 36 \times 9$.

To provide more details on the temperature dependence of $\Delta F(\pi)$ with fixed h_z, we choose several h_z in the "Y"
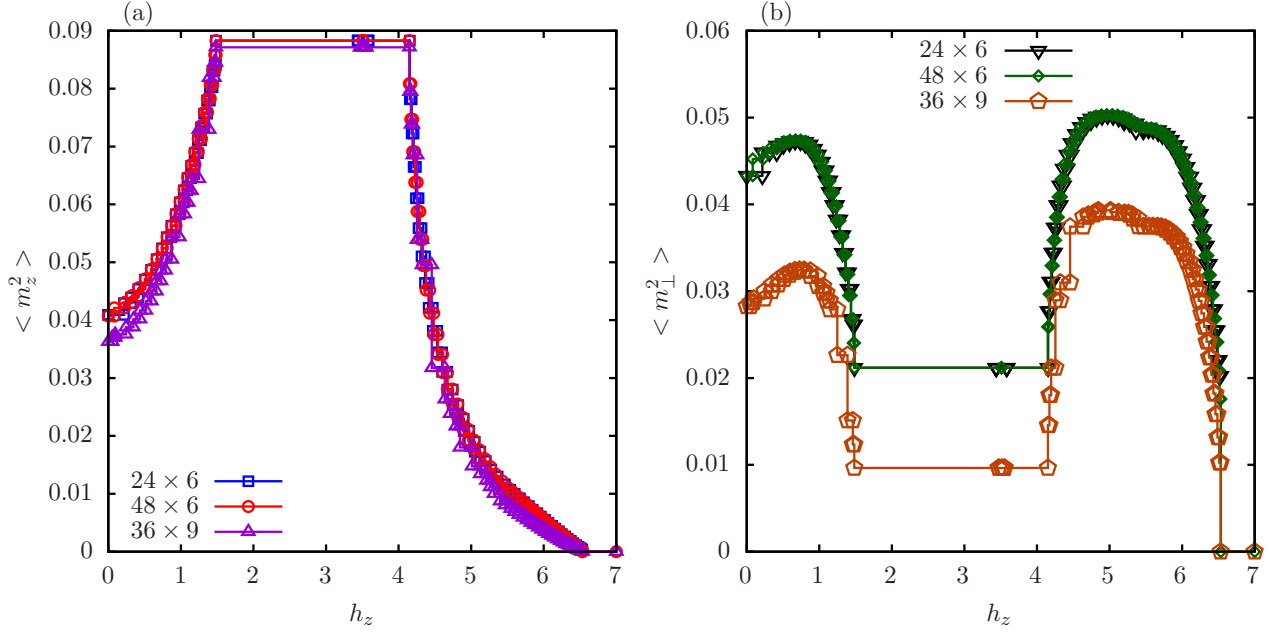
FIG. S7. (a) the $\langle m_z^2 \rangle$ and (b) the $\langle m_\perp^2 \rangle$ obtained for various h_z on lattices of $L_x \times L_y = 24 \times 6$, 48×6 and 36×9.

and "V" supersolid states and show the $\Delta F(\pi)$ as a function of T in Fig. S8. For the "Y" supersolid states at $h_z = 0.56$ and 0.75 starting at the lowest temperature, the $\Delta F(\pi)$ has a slight increase as T increases which may be due to numerical convergence for the given bond dimension at very low temperatures. Then the $\Delta F(\pi)$ decreases over T as the spin supersolid state transits into the high temperature state. The phase transition is estimated by the derivative of $\Delta F(\pi)$ with respect to T, as shown in the inset of Fig. S8, and we find that the derivative of $\Delta F(\pi)$ has a peak near $T = 0.1$. For the "V" supersolid states at $h_z = 4.69$ and 4.88, the temperature evolution of $\Delta F(\pi)$ is qualitatively the same, except for a smaller transition temperature.

V.   LINEAR SPIN WAVE THEORY

The spin wave theory provides a good approximation of the isolated modes of the magnon excitations. The magnon dispersions are carried out using a semi-classical model starting from the ground states for various magnetic fields. Under finite magnetic fields the ground states consist of the "Y" supersolid, the UUD, and the "V" supersolid states, where the spins are assumed to align in the xz plane with three-site unit cell labeled by $v = 1, 2, 3$ and θ_v as the angle between the z axis and the spin. Assuming that the magnetic fields are applied in the z direction, for the UUD state we have $\theta_1 = \theta_2 = 0, \theta_3 = \pi$. For the "Y" supersolid state we have $\theta_1 = -\theta_2, \theta_3 = \pi$, and for the "V" supersolid state we have $\theta_1 = \theta_2$; see illustrations in Fig. S9.

The $\theta_{1,2,3}$ can be determined by minimizing the classical energy in a unit cell which is given as

$$E(\theta_1, \theta_2, \theta_3) = \frac{3}{2} J \sum_{v \neq v'} (S_v^x \cdot S_{v'}^x + S_v^y \cdot S_{v'}^y + \Delta_z S_v^z \cdot S_{v'}^z) - h_z \sum_v S_v^z \tag{S1}$$

where $\mathbf{S}_v$ depends on θ_v through the rotation given in below [47]. The spin operators are rotated before mapped onto a set of boson creation and annihilation operators with the Holstein-Primakoff transformation [74]. The rotation in xz plane is given as

$$R(\theta_v) = \begin{bmatrix} \cos\theta_v & 0 & \sin\theta_v \\ 0 & 1 & 0 \\ -\sin\theta_v & 0 & \cos\theta_v \end{bmatrix}, \tag{S2}$$

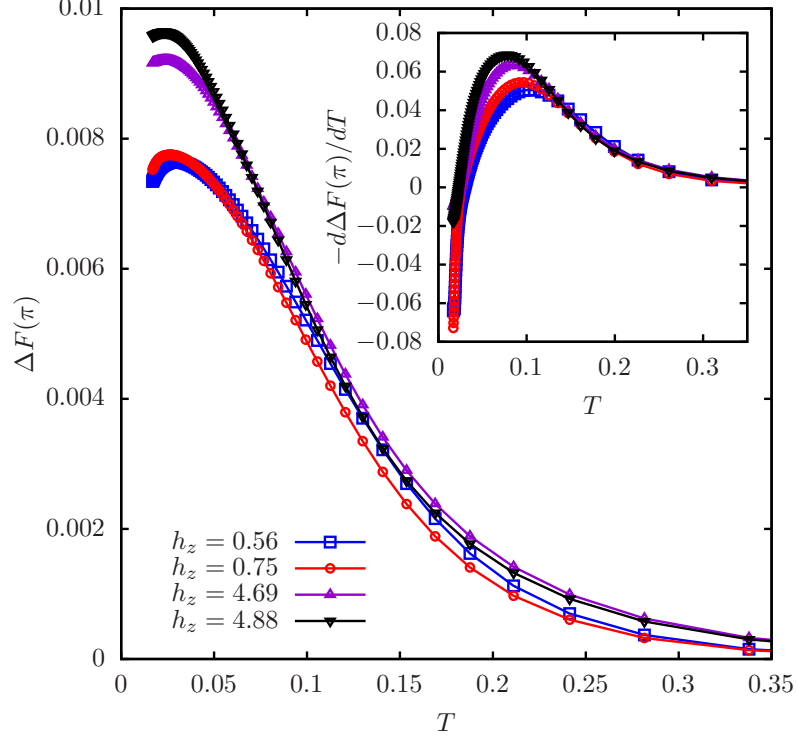$$\mathbf{S}_v = R(\theta_v) \cdot \widetilde{\mathbf{S}}_v, \tag{S3}$$

FIG. S8. The $\Delta F(\pi)$ for finite temperatures T obtained for various h_z on the lattice of $L_x \times L_y = 18 \times 6$. The inset shows derivative of $\Delta F(\pi)$ with respect to T.
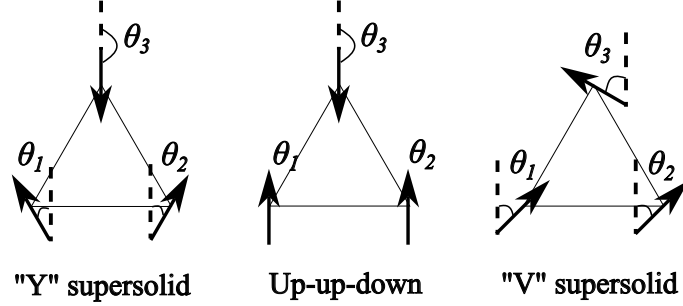

FIG. S9. The illustration of classical spin configuration for various ground states under magnetic fields.

and the Holstein-Primakoff transformation is given in Eq. S4

$$
\begin{aligned}
\widetilde{S}^+_{\mathbf{u},v} &= \sqrt{2S - a^\dagger_{\mathbf{u},v} a_{\mathbf{u},v}}\, a_{\mathbf{u},v}, \\
\widetilde{S}^-_{\mathbf{u},v} &= a^\dagger_{\mathbf{u},v} \sqrt{2S - a^\dagger_{\mathbf{u},v} a_{\mathbf{u},v}}, \\
\widetilde{S}^z_{\mathbf{u},v} &= S - a^\dagger_{\mathbf{u},v} a_{\mathbf{u},v}.
\end{aligned}
\tag{S4}
$$

Here, we consider the whole system where the spin operators $\widetilde{S}^+_{\mathbf{u},v}$ and boson annihilation operators $a_{\mathbf{u},v}$ are labeled by the unit cell index $\mathbf{u}$, and the site index v within the unit cell.

The Fourier transformation to the momentum space is defined as $a_{\mathbf{u},v} = \frac{1}{\sqrt{N/3}} \sum_{\mathbf{k}} e^{i\mathbf{k}\cdot\mathbf{u}} a_{\mathbf{k},v}$, and the corresponding Hamiltonian becomes

$$H = \sum_{\mathbf{k}} \Phi_{\mathbf{k}}^{\dagger} [H]_{\mathbf{k}} \Phi_{\mathbf{k}}, \tag{S5}$$

$$\Phi_{\mathbf{k}}^{\dagger} = (a_{\mathbf{k},1}^{\dagger}, a_{\mathbf{k},2}^{\dagger}, a_{\mathbf{k},3}^{\dagger}, a_{-\mathbf{k},1}, a_{-\mathbf{k},2}, a_{-\mathbf{k},3})$$

where $[H]_{\mathbf{k}}$ is a 6×6 matrix. Here we only consider terms involving two operators, and the lattice spacing is set to 1 for simplicity. We perform the Bogoliubov transformation where the quasi-particle excitations naturally obey the bosonic commutation relations. For a generic quadratic bosonic Hamiltonian, the excitations can be obtained by diagonalizing the dynamical matrix $[H]_{\mathbf{k}}^{dyn}$ which is defined as [90]

$$[H]_{\mathbf{k}}^{dyn} = \mathbb{G}[H]_{\mathbf{k}}, \tag{S6}$$

$$\mathbb{G} = \begin{bmatrix} \mathbf{1} & 0 \\ 0 & -\mathbf{1} \end{bmatrix}$$

where $\mathbf{1}$ is a 3-dimensional identity matrix. Numerically, one can also follow the steps by Colpa [91] to obtain the magnon excitations of this type of Hamiltonian; also see discussions in Refs. [90, 92, 93].

Solving $[H]_{\mathbf{k}}^{dyn}$ for the eigenvalues $\varepsilon(\mathbf{k})$, we arrive at three positive energy dispersions. Other three negative dispersions are neglected. The three magnon dispersions are plotted in the main text with different h_z for the corresponding state.